(Preprint) AAS 26-749

CASCADED CONTROL ARCHITECTURE FOR SPACECRAFT WITH ARM-MOUNTED THRUSTERS USING REACTION TORQUE COMPENSATION

William R. Schwend,[*] Hanspeter Schaub[†]

A cascaded control architecture for spacecraft with arm-mounted thrusters is presented. The goal is to maneuver in close proximity to another satellite. It explicitly incorporates a prescribed hub-torque term within the inner servo loop to cancel instantaneous reaction torques induced by joint motion. This enables continuous attitude pointing during rapid arm reconfiguration where the thrusters are positioned into a configuration for the next burn. This arm-mounted approach reduces the required number of thrusters and eliminates the need for thrust cancellation strategies common in fixed thruster configurations. However, dynamics and control challenges with time-dependent inertia must be overcome. The coupled spacecraft–arm dynamics are formulated and used to design feedback control laws for the relative motion, attitude pointing, and joint actuation. The main spacecraft bus must maintain a prescribed orientation relative to the neighboring spacecraft during the arm motions. The stability and performance of the overall control system are discussed, and numerical simulations demonstrate its ability to achieve full six-degree-of-freedom regulation while highlighting the importance of compensating for arm-induced reaction torques.

INTRODUCTION

With the growth of more complex mission concepts, the ability to launch fully operational spacecraft on a single rocket is rapidly becoming infeasible[1] requiring on-orbit assembly. Additionally, the need to extend mission lifetimes, repair broken components, build new spacecraft, and upgrade on-orbit legacy systems has led to In-Orbit Servicing, Assembly, and Manufacturing (ISAM) capabilities becoming a key priority for both commercial and national space interests alike.[2,3] Similarly, the steady growth of on-orbit debris has driven interest in space debris removal technologies.[4] Two technologies shared between these interests include the development of close-proximity operations capabilities and the integration of multi-degree-of-freedom (DOF) arms onto spacecraft. Robotic arms have been used in conjunction with proximity operations since the servicing missions to the Hubble Space Telescope conducted by the Space Shuttle.[5] The OSAM-1 mission, formerly under development by NASA[‡], and the proposed ClearSpace-1 mission by ClearSpace SA[§], Fig. 1, similarly seek to utilize robotic arms to conduct ISAM and space debris removal operations, respectively.

Traditionally, the control of spacecraft conducting proximity operations has been implemented using fixed thruster configurations, often with the assistance of on-board momentum management devices such as reaction wheels (RWs), control moment gyroscopes (CMGs), and variable speed CMGs (VSCMGs).[6–10] Utilizing these fixed thruster configurations allows for a variety of well established thruster allocation algorithms to be

[*]PhD Student, Ann and H.J. Smead Department of Aerospace Engineering Science, University of Colorado, Boulder, 80303, AIAA Student Member

[†]Distinguished Professor and Department Chair, Schaden Leadership Chair, Ann and H.J. Smead Department of Aerospace Engineering Sciences, University of Colorado, Boulder, 80303, Fellow of AIAA and AAS

[‡]https://www.nasa.gov/centers-and-facilities/goddard/nasas-robotic-osam-1-mission-completes-its-critical-design-review/

[§]https://www.esa.int/ESA_Multimedia/Images/2025/04/ESA_s_ClearSpace-1_prepares_to_deorbit_ESA_s_Proba-1_satellite

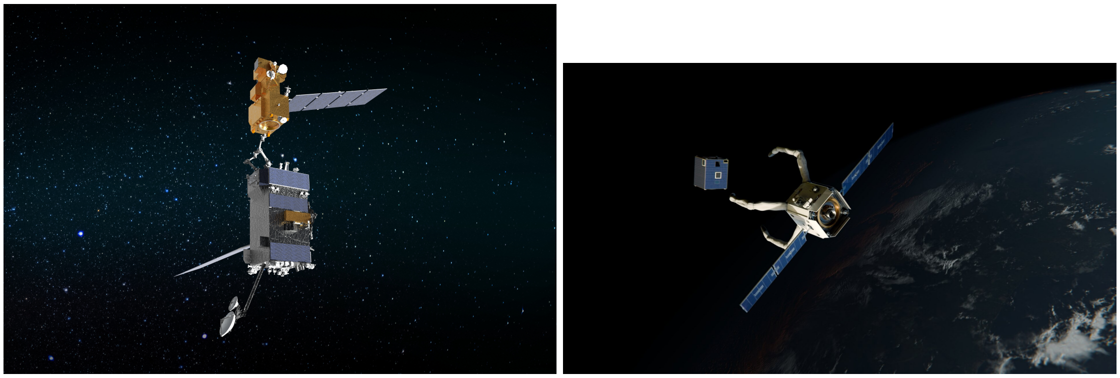

(a) OSAM-1 mission concept art[‡] (b) ClearSpace-1 mission concept art[§]

Figure 1: Concept figures of spacecraft using robotic arms in proximity operations.

used including: table lookup, Moore-Penrose pseudoinverse based methods, linear programming, quadratic programming, mixed integer linear programming, and Lyapunov theory based methods.[10–13] These fixed thruster configurations are not without limitations, however. To achieve 6-DOF control, thruster configurations of eight or more thrusters are typically required. This results in a large amount of mass being added to the spacecraft due to the additional thrusters and associated fuel systems and often requires additional thrusting to counteract undesired control wrenches produced by non-ideal thruster geometry.[14]

Recently, spacecraft such as the Northrop Grumman Mission Extension Vehicle (MEV)[*] and Astroscale's Life Extension In-orbit (LEXI)[†], Fig. 2, have been proposed. These spacecraft seek to take advantage of the presence of robotic arms on-board ISAM and space debris removal spacecraft by attaching thrusters at the ends of the arms. This allows less thrust to be used for the same control wrench as the thrusters can be reconfigured eliminating the need for thrust cancellation.[15–22] Additionally, the number of thrusters on the spacecraft can be reduced to just two,[18–20] potentially reducing the required mass of the thruster systems.

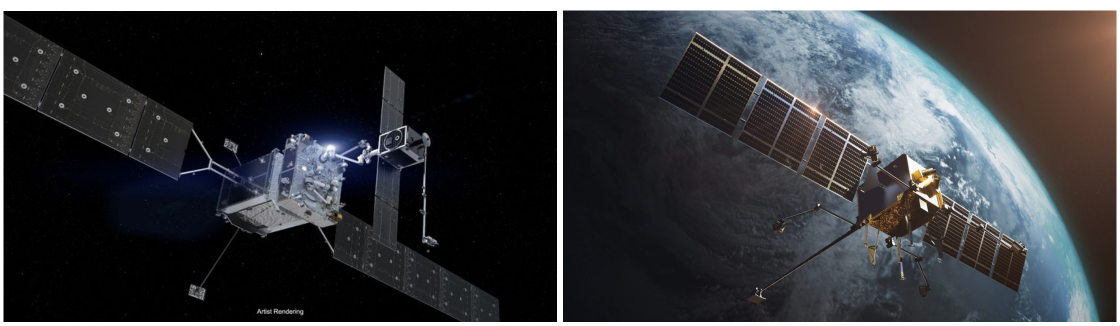

(a) MEV mission concept art[*] (b) LEXI mission concept art[‡]

Figure 2: Concept figures of spacecraft with thrusters mounted on robotic arms.

Incorporating robotic arms into spacecraft significantly increases the complexity of control design due to the dynamic coupling between arm motion and hub dynamics.[23–25] Significant work in the field of space robotics has addressed the design of control systems for such spacecraft,[26–32] but these efforts primarily fo-

[*]https://news.northropgrumman.com/satellites/northrop-grummans-spacelogistics-continues-revolutionary-satellite-life-extension-work-with-sale-of-third-mission-extension-pod
[†]https://www.astroscale.com/en/missions/lexi-p
[‡]https://www.astroscale-us.com/en/news/astroscale-israel-completes-construction-of-new-computer-vision-robotics-lab-and-clean-room

cus on the coordinated manipulator-spacecraft control or momentum management rather than exploiting the arms as thruster mounting points. Recent studies have investigated the use of arm mounted thrusters for station keeping control and momentum management of geostationary Earth orbit (GEO) spacecraft.[15–19] The slow mission timescale of these GEO maneuvers permits lengthy arm reconfigurations, allowing traditional RW-based attitude control to absorb the resulting disturbances. In contrast, proximity-operation missions require rapid arm reconfigurations and tighter pointing requirements. Reference 20 introduces a loop dynamics formulation that uses thrusters mounted on robotic arms to conduct proximity operations with no additional momentum management devices, allowing for hub attitude deviations during arm motion. More recently, Ref. 21 develops a task-space controller that uses dynamic decoupling and attitude regulation to perform spacecraft center-of-mass (CoM) translation with an end effector mounted thruster while regulating the spacecraft's attitude. By explicitly considering base-attitude regulation during end-effector alignment, their work reinforces the importance of preserving pointing constraints while exploiting arm-mounted thrusters for proximity-operation maneuvers. Finally, Ref. 22 introduces a prescribed hub torque to counteract reaction torques generated by arm motion in real time, though the analysis is limited to planar dynamics with single-DOF arms.

While these prior studies have examined spacecraft control using arm-mounted thrusters, none incorporate an inner-loop solution to explicitly prevent hub angular accelerations resulting from arm motion. Works such as Refs. 15–19 either neglect the reaction torques that joint articulation introduces or combine the torques with environmental effects as part of a low-frequency disturbance on the hub. Reference 20 corrects for the resulting attitude deviations during thruster firing but does not prevent them from occurring during arm motion. Reference 21 utilizes coordinated manipulator and reaction-wheel torques to regulate the attitude of the spacecraft during arm motion, but does not formulate the reconfiguration phase as an explicit hub inverse-dynamics problem or compute the hub torque required to enforce zero hub angular acceleration. Additionally, Ref. 21 uses the end-effector thruster only for CoM translational motion rather than full 6-DOF spacecraft control.

This paper extends prior efforts through the novel incorporation of a prescribed hub-torque term into a cascaded 6-DOF control architecture for spacecraft employing arm-mounted thrusters while conducting proximity operations. The proposed formulation explicitly computes the hub torque required to enforce zero hub angular acceleration during rapid multi-DOF arm reconfiguration, thereby compensating for instantaneous arm-induced reaction torques in real time. This allows the hub to maintain stability and sensor line-of-sight (LOS) throughout arm articulation, even during fast-paced maneuvers. In addition, this work quantifies the prescribed hub-torque demands associated with the rapid reconfiguration necessitated by proximity operations, evaluates the effect of limiting the available prescribed torque to levels representative of practical momentum-exchange devices, and assesses the validity of the hub-inertia-dominant modeling assumption used by the outer-loop attitude controller over a range of arm-to-hub mass ratios. The remainder of this paper first introduces the coupled manipulator-spacecraft dynamics and summarizes the cascaded control architecture used for arm-mounted-thruster control. The outer-loop control and allocation methods are then developed, followed by the inner-loop controller and prescribed-hub-torque approach used to compensate manipulator-induced reaction torques. The paper concludes with numerical simulation results and a summary of the primary findings.

NUMERICAL SYSTEM MODELING

The spacecraft considered in this work is comprised of a rigid central hub with attached lightweight multi-DOF robotic arms. The spacecraft's thrusters are mounted on these robotic arms. The example configuration in Fig. 3 has two 4-DOF arms with a single thruster at the end of each arm, though the formulation allows for an arbitrary number of arms, joints, and thrusters. The rigid hub has a CoM located at point B_c, while the full spacecraft CoM is located at point C. Each revolute joint has a joint frame $\mathcal{J}_i$ centered at point J_i and spin axis $\hat{s}_i$. Each fixed length arm link has a CoM at point A_{i_c} and an arm frame $\mathcal{A}_i$ centered at point A_i. Finally, each thruster has a thrust force direction $\hat{f}_i$ and thruster frame $\mathcal{T}_i$ centered at point T_i. The thrusters generate external forces and torques on the overall system, while additional external control torques may be directly applied to the spacecraft hub during joint actuation. The equations of motion presented in this section form the basis for the control development presented later in this paper.

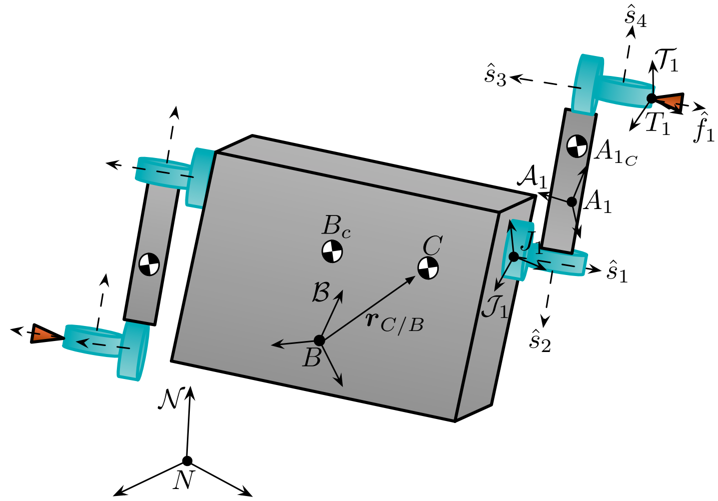

Figure 3: Example spacecraft with a rigid hub and two 4-DOF arms with end-mounted thrusters

The coupled rigid-body dynamics of the spacecraft and attached robotic arms are represented using the standard generalized-coordinate multi-body formulation[33] as shown in Eq. (1). These dynamics may be simulated using any general multi-body dynamics solver. For the control discussed later in this paper, the solver must provide access to the full system mass matrix and the non-actuator generalized bias forces arising from Coriolis, centrifugal, gravitational, and other configuration-dependent effects. For the results presented in this work, the open-source physics engine MuJoCo[34] is selected as the dynamics simulator. MuJoCo implements Featherstone-style articulated rigid-body dynamics with additional handling for constraints and contact physics.

$$[M(\boldsymbol{q})]\ddot{\boldsymbol{q}} + \boldsymbol{C}(\boldsymbol{q}, \dot{\boldsymbol{q}}) = \boldsymbol{\tau} \tag{1}$$

In Eq. (1)$[M(\boldsymbol{q})]$ is the state-dependent system mass matrix and $\boldsymbol{\tau}$ is the vector of generalized forces acting on the system corresponding to generalized coordinates $\boldsymbol{q}$. The coordinates used for the remainder of this paper are $\boldsymbol{q} = [\boldsymbol{r}_{B/N}, \boldsymbol{\sigma}_{B/N}, \boldsymbol{\theta}]^T$, $\dot{\boldsymbol{q}} = [\dot{\boldsymbol{r}}_{B/N}, \boldsymbol{\omega}_{B/N}, \dot{\boldsymbol{\theta}}]^T$, and $\ddot{\boldsymbol{q}} = [\ddot{\boldsymbol{r}}_{B/N}, \dot{\boldsymbol{\omega}}_{B/N}, \ddot{\boldsymbol{\theta}}]^T$. The vector $\boldsymbol{r}_{B/N}$ is the position vector of the body frame $\mathcal{B}$ origin, B, of the hub with respect to the inertial frame $\mathcal{N}$ origin, N. The matrix $\boldsymbol{\sigma}_{B/N}$ contains the Modified Rodrigues Parameters (MRP) set describing the orientation of $\mathcal{B}$ relative to $\mathcal{N}$ while $\boldsymbol{\omega}_{B/N}$ is the angular velocity of $\mathcal{B}$ relative to $\mathcal{N}$.[35–38] The vector $\boldsymbol{\theta} \in \mathbb{R}^{N_J}$ denotes the current joint angles for each of the N_J joints in the robotic arms. Using these coordinates the vector $\boldsymbol{C}$ can be broken down as

$$\boldsymbol{C} = \begin{bmatrix} \boldsymbol{C}_T \\ \boldsymbol{C}_R \\ \boldsymbol{C}_\theta \end{bmatrix} \tag{2}$$

where $\boldsymbol{C}_T \in \mathbb{R}^3$ is the translational component of the generalized bias force associated with the hub, $\boldsymbol{C}_R \in \mathbb{R}^3$ is the corresponding rotational component, and $\boldsymbol{C}_\theta \in \mathbb{R}^{N_J}$ contains the joint-space bias torques. The vector $\boldsymbol{\tau}$ can be rewritten as

$$\boldsymbol{\tau} = \begin{bmatrix} \boldsymbol{F}_{\text{thr}} \\ \boldsymbol{L}_{\text{thr}} + \boldsymbol{\tau}_{\text{pre}} \\ \boldsymbol{\tau}_{\text{thr}} + \boldsymbol{u}_J \end{bmatrix} \tag{3}$$

with $\boldsymbol{F}_{\text{thr}} \in \mathbb{R}^3$ being the thruster control force acting on the spacecraft hub. $\boldsymbol{L}_{\text{thr}} \in \mathbb{R}^3$ is the thruster control torque acting on the spacecraft hub and $\boldsymbol{\tau}_{\text{pre}} \in \mathbb{R}^3$ represents a control torque applied directly to the hub to counteract reaction torques during joint actuation, negating any hub angular accelerations. The set $\boldsymbol{\tau}_{\text{thr}} \in \mathbb{R}^{N_J}$ represents the torque on the joint that results from thruster firing while $\boldsymbol{u}_J \in \mathbb{R}^{N_J}$ is the vector of control torques acting on the joints.

The system mass matrix can also be represented using submatrices as

$$[M] = \begin{bmatrix} M_{TT} & M_{TR} & M_{T\theta} \\ M_{TR}^T & M_{RR} & M_{R\theta} \\ M_{T\theta}^T & M_{R\theta}^T & M_{\theta\theta} \end{bmatrix} \tag{4}$$

with $M_{TT}, M_{TR}, M_{RR} \in \mathbb{R}^{3\times3}$, $M_{T\theta}, M_{R\theta} \in \mathbb{R}^{3\times N_J}$ and $M_{\theta\theta} \in \mathbb{R}^{N_J\times N_J}$. These equations of motion expose the coupling between joint articulation and hub dynamics. The control architecture developed in the next section exploits this structure to maintain pointing performance while reconfiguring the robotic arms.

CONTROL ARCHITECTURE

During proximity operations, the deputy spacecraft must regulate its relative translation and attitude while simultaneously reconfiguring its robotic arms to satisfy control authority requirements. As illustrated by the representative inspection mission in Fig. 4, the narrow field-of-view (FOV) of the deputy's sensing instruments demands precise pointing to maintain continuous LOS to the chief spacecraft. However, articulation of the robotic arms produces reaction torques on the deputy's hub, which can drive the hub attitude away from these pointing constraints. Consequently, the control architecture must explicitly account for, and counteract, these reaction torques to ensure pointing performance throughout the mission.

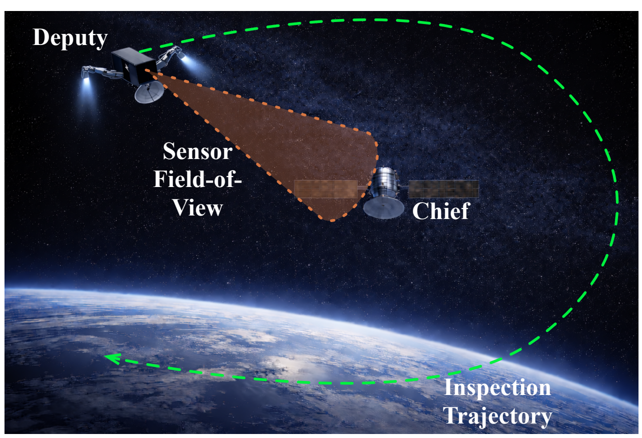

Figure 4: Concept inspection mission using a deputy spacecraft with arm-mounted thrusters.

To address these coupled requirements, a cascaded control architecture is adopted, as shown in Fig. 5.

The outer control loop computes the required control wrench $\boldsymbol{u}$, from which the desired joint angles $\boldsymbol{\theta}^*$ and thruster firing times $\boldsymbol{t}^*_{\text{fire}}$ are generated. The inner control loop consists of two phases: (1) joint articulation, wherein the robotic joints track their commanded configurations, and (2) thruster firing, during which the arm-mounted thrusters realize the outer-loop wrench.

During the joint articulation phase, $\boldsymbol{\tau}_{\text{pre}}$ is applied to the spacecraft hub to cancel the reaction torques induced by joint motion in real time. This torque enforces zero hub angular acceleration during arm reconfiguration, thereby preventing the commanded joint motion from disturbing the hub attitude while the arms reconfigure. The explicit inclusion of this prescribed hub torque within the inner control loop is the central contribution of this study, as it enables stable hub pointing despite rapid and dynamically coupled arm motion.

It is important to note that in this work $\boldsymbol{\tau}_{\text{pre}}$ is treated as an ideal control input rather than being generated by a specific actuator (e.g. RWs, CMGs, or VSCMGs). This abstraction is intentional, as the objective of this study is to isolate and characterize the instantaneous hub torque requirements arising from manipulator-hub dynamic coupling, independent of actuator implementation details. In particular, momentum storage, accumulation, and desaturation management are not considered here, as they constitute a higher-level resource allocation problem separate from the coupled rigid–manipulator dynamics under investigation. Incorporation of representative actuator models and momentum management strategies is therefore reserved for future work.

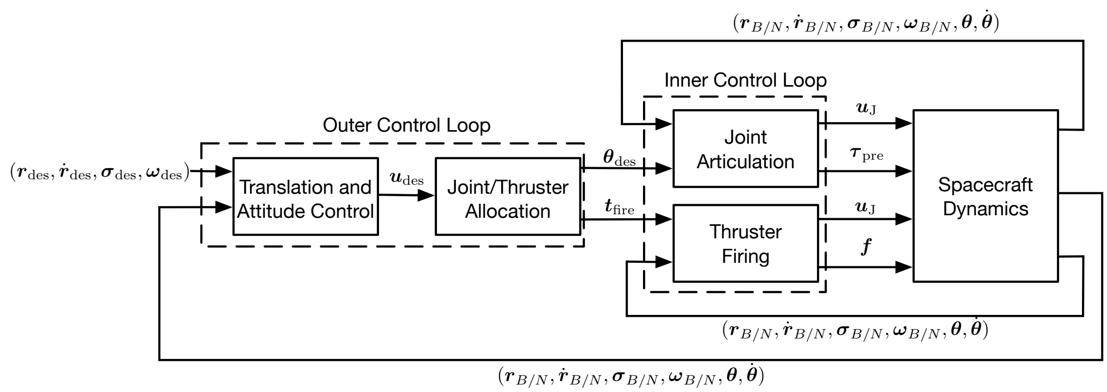

Figure 5: Cascaded control loop design

OUTER CONTROL LOOP

The objective of the outer control loop is to drive the spacecraft to track the desired reference states. By exploiting the separation of time scales between the outer and inner control loops, and taking advantage of the asymptotic stability of the joint actuation control in the *Inner Control Loop* section, the spacecraft may be treated as a rigid body for the purpose of computing the required outer-loop control wrench. This approximation enables the outer loop to focus on achieving the mission-level objectives, while the inner loop handles the rapid configuration changes required to realize the commanded wrench.

Approach and inspection phases of in-space servicing, assembly, and manufacturing (ISAM) or debris-removal missions often require long-duration, high-accuracy relative-motion control. The ADRAS-J mission, for example, maneuvered to within approximately 15 m of a tumbling rocket body during its inspection operations.[39] Such scenarios emphasize the need for precise control of the deputy spacecraft's relative position and attitude. Because translational relative motion is governed strictly by the location of the system CoM, the outer-loop controller in this work regulates the state vector $[\boldsymbol{r}_d, \boldsymbol{\sigma}_{B/N}, \dot{\boldsymbol{r}}_d, \boldsymbol{\omega}_{B/N}]^T$ where $\boldsymbol{r}_d$ denotes the inertial position of the deputy system CoM.

Using the system CoM as the reference point offers a key advantage: it effectively decouples translational motion from hub rotational dynamics, even in the presence of significant internal arm motion. As a result, the desired control wrench decomposes naturally into two components, one governing translational motion of the CoM and the other governing hub attitude.

The computed control wrench is subsequently passed to the control allocation stage, where the commanded forces and torques are mapped into desired joint configurations and thruster firing durations. These allocations are then executed by the inner-loop controllers, which actuate the robotic arms and thrusters to realize the commanded wrench.

Translational Control

To derive the translational control law, the system CoM position and velocity must first be expressed in terms of the hub state and joint-dependent arm geometry. The position of the deputy spacecraft system CoM is first determined through

$$\boldsymbol{r}_d = \boldsymbol{r}_{B/N} + \boldsymbol{r}_{C/B} \tag{5}$$

with

$$\boldsymbol{r}_{C/B} = \frac{m_{\text{hub}}\boldsymbol{r}_{B_c/B} + \sum_{i=1}^{N_a} m_{a_i}\boldsymbol{r}_{A_{i_c}/B}}{m_d} \tag{6}$$

Here, m_{hub} is the mass of the spacecraft hub and m_{a_i} is the mass of the ith arm segment and N_a is the total number of arm segments. The variable $\boldsymbol{r}_{B_c/B}$ is the position vector from point B to the hub CoM and $\boldsymbol{r}_{A_{i_c}/B}$ is the position vector from point B to the ith arm segment's CoM. The total spacecraft mass m_d is defined as

$$m_d = m_{\text{hub}} + \sum_{i=1}^{N_a} m_{a_i} \tag{7}$$

The velocity of the deputy system CoM follows directly from differentiating Eq. (5)

$$\dot{\boldsymbol{r}}_d = \dot{\boldsymbol{r}}_{B/N} + \dot{\boldsymbol{r}}_{C/B} \tag{8}$$

where $\dot{\boldsymbol{r}}_{C/B}$ is found using the transport theorem[38] as

$$\dot{\boldsymbol{r}}_{C/B} = \boldsymbol{r}'_{C/B} + \boldsymbol{\omega}_{B/N} \times \boldsymbol{r}_{C/B} \tag{9}$$

where the prime denotes a time derivative of the vector as seen by the $\mathcal{B}$ frame. Because each arm segment is rigid and of fixed length, and $\boldsymbol{r}_{B_c/B}$ is constant, the only contribution to $\boldsymbol{r}'_{C/B}$ arises from the joint-driven motion of the arm link CoMs, giving

$$\boldsymbol{r}'_{C/B} = \frac{\sum_{i=1}^{N_a} m_{a_i}(\boldsymbol{\omega}_{A_i/B} \times \boldsymbol{r}_{A_{i_c}/B})}{m_d} \tag{10}$$

where $\boldsymbol{\omega}_{A_i/B}$ is the angular velocity between the ith $\mathcal{A}$ frame and the $\mathcal{B}$ frame. With these expressions for the system CoM kinematics, the translational dynamics of the chief $\boldsymbol{r}_c$ and deputy spacecraft CoMs follow directly from Newton's second law as

$$m_c\ddot{\boldsymbol{r}}_c = \boldsymbol{F}_c \tag{11a}$$

$$m_d\ddot{\boldsymbol{r}}_d = \boldsymbol{F}_d + \boldsymbol{F}_{\text{thr}} \tag{11b}$$

where the chief spacecraft is in an uncontrolled orbit and the deputy is being controlled to maintain the desired relative orbit. The vectors $\boldsymbol{F}_c$ and $\boldsymbol{F}_d$ are the sum of all external, non-control forces acting on the chief and deputy, respectively. The desired deputy position $\boldsymbol{r}^*_d$ is defined relative to the chief spacecraft as

$$\boldsymbol{r}^*_d = \boldsymbol{r}_c + \boldsymbol{\rho}^* \tag{12}$$

where $\boldsymbol{\rho}^*$ is the vector pointing from the chief position to the desired deputy position. The corresponding desired CoM dynamics then satisfy

$$m_d \ddot{\boldsymbol{r}}_d^* = \boldsymbol{F}_d^* + \boldsymbol{F}_{\text{thr}}^* \tag{13}$$

Here $\boldsymbol{F}_d^*$ is the sum of all external, non-control forces acting on the desired deputy, and $\boldsymbol{F}_{\text{thr}}^*$ is the ideal control force required to keep the deputy on the desired relative orbit. Following the development of the cartesian coordinate continuous feedback control law in Ref. 38 the position tracking error is defined as

$$\Delta \boldsymbol{r} = \boldsymbol{r}_d - \boldsymbol{r}_d^* \tag{14}$$

To track the desired trajectory, a Lyapunov candidate function is constructed using this error vector and its derivative:

$$V(\Delta \boldsymbol{r}, \Delta \dot{\boldsymbol{r}}) = \frac{m_d}{2} \Delta \dot{\boldsymbol{r}}^T \Delta \dot{\boldsymbol{r}} + \frac{1}{2} \Delta \boldsymbol{r}^T [K_T] \Delta \boldsymbol{r} \tag{15}$$

where $[K_T] \in \mathbb{R}^{3\times3}$ is a positive definite proportional gain matrix. Taking the time derivative of V, substituting in Eqs. (11b) and (13), and enforcing the condition

$$\dot{V} = -\Delta \dot{\boldsymbol{r}}^T [P_T] \Delta \dot{\boldsymbol{r}} \tag{16}$$

where $[P_T] \in \mathbb{R}^{3\times3}$ is a positive definite derivative gain matrix, yields a control law that renders the tracking error dynamics globally asymptotically stable (see the Appendix for the corresponding Lyapunov stability proof).

$$\boldsymbol{F}_{\text{thr}} = -(\boldsymbol{F}_d - \boldsymbol{F}_d^*) - [K_T] \Delta \boldsymbol{r} - [P_T] \Delta \dot{\boldsymbol{r}} + \boldsymbol{F}_{\text{thr}}^* \tag{17}$$

Rotational Control

Having determined the desired translational force, we now establish the rotational component of the control wrench. Consistent with the architectural assumptions introduced in the *Control Architecture* section, the spacecraft is modeled as a rigid body without internal momentum exchange devices, and the hub torques required to counteract the effects of arm motion are treated as ideal control inputs. The remaining control torques are produced exclusively by the thrusters. Under these assumptions, the rotational equations of motion follow the formulation in Ref. 38 and take the form

$$[I] \dot{\boldsymbol{\omega}}_{B/N} = -[\tilde{\boldsymbol{\omega}}][I] \boldsymbol{\omega}_{B/N} + \boldsymbol{L}_{\text{thr}} + \boldsymbol{L}_{\text{ext}} \tag{18}$$

where $[I]$ denotes the full spacecraft inertia tensor about point B, $[\tilde{\boldsymbol{\omega}}]$ is the skew-symmetric matrix representation of the angular velocity vector $\boldsymbol{\omega}_{B/N}$, and the vector $\boldsymbol{L}_{\text{ext}}$ is the sum of all external, non-control torques acting on the spacecraft.

Because the rotational control torque is used by the joint allocation algorithm, as discussed later in this section, to determine the required arm configuration, the full inertia tensor $[I]$, which is dependent on that configuration, cannot be treated as known a priori when computing the control torque. This implicit coupling introduces a circular dependence between inertia evaluation and torque computation, because accurate evaluation of $[I]$ would require knowledge of the arm configuration selected to realize the commanded torque. Numerous rotation control laws could be employed to determine this torque without perfect knowledge of $[I]$, including inertia free formulations and adaptive schemes.[40,41] For this work, the classical MRP feedback control law is selected due to its relative simplicity and demonstrated robustness to inertia modeling errors.[38] For this controller an estimate of $[I]$ is used in the form of the fixed spacecraft hub inertia about point B, $[I_H]$. This approximation is motivated by the design regime of interest, in which the central hub mass significantly exceeds the total arm mass. Under this assumption, $[I_H]$ represents the dominant contribution to the total inertia, and the configuration dependent contributions from the arms constitute a bounded modeling error. The control torque follows as

$$\boldsymbol{L}_{\text{thr}} = -K_R \delta \boldsymbol{\sigma} - [P_R] \delta \boldsymbol{\omega} + [I_H](\dot{\boldsymbol{\omega}}^* - [\tilde{\boldsymbol{\omega}}] \boldsymbol{\omega}^*) + [\tilde{\boldsymbol{\omega}}][I_H] \boldsymbol{\omega}_{B/N} - \boldsymbol{L}_{\text{ext}} \tag{19}$$

where K_R is a positive scalar proportional gain for attitude feedback, and $[P_R] \in \mathbb{R}^{3\times3}$ is a positive-definite derivative gain matrix. The vector $\delta\boldsymbol{\sigma}$ is a measurement of the attitude error and the angular velocity error $\delta\boldsymbol{\omega}$ is defined using the desired angular velocity of the spacecraft $\boldsymbol{\omega}^*$ through

$$\delta\boldsymbol{\omega} = \boldsymbol{\omega}_{B/N} - \boldsymbol{\omega}^* \tag{20}$$

While the Lyapunov stability proof for the control law assumes exact knowledge of the inertia tensor, prior studies and simulation evidence suggest that the controller maintains satisfactory performance under moderate inertia mismatch.[38] The impact of inertia mismatch on closed-loop performance is evaluated in a later section, where the hub-to-arm mass ratio is varied while maintaining translational and joint performance.

Joint and Thruster Allocation

Once the required control wrench is computed, it must be mapped into feasible joint configurations and thruster commands that the inner loop can execute. This wrench is expressed as

$$\boldsymbol{u} = \begin{bmatrix} \boldsymbol{F}_{\text{thr}} \\ \boldsymbol{L}_{\text{thr}} \end{bmatrix} \tag{21}$$

Following the approach by Ref. 18, the desired joint angles $\boldsymbol{\theta}^* \in \mathbb{R}^{N_J}$ and N_T thruster force magnitudes $\boldsymbol{f}^* \in \mathbb{R}^{N_T}$ are determined by solving the constrained nonlinear optimization problem defined through

$$\min_{\boldsymbol{\theta}^*, \boldsymbol{f}^*} (\boldsymbol{u} - \boldsymbol{u}_{\text{ctl}}(\boldsymbol{\theta}^*, \boldsymbol{f}^*))^T \boldsymbol{W}_u (\boldsymbol{u} - \boldsymbol{u}_{\text{ctl}}(\boldsymbol{\theta}^*, \boldsymbol{f}^*)) + \boldsymbol{W}_f^T \boldsymbol{f}^* \tag{22}$$

subject to

$$\begin{aligned} \boldsymbol{\theta}_{\text{min}} \leq \boldsymbol{\theta}^* \leq \boldsymbol{\theta}_{\text{max}} \\ \boldsymbol{0} \leq \boldsymbol{f}^* \leq \boldsymbol{f}_{\text{max}} \end{aligned} \tag{23}$$

Here, $\boldsymbol{W}_u \in \mathbb{R}^{6\times6}$ and $\boldsymbol{W}_f \in \mathbb{R}^{N_T}$ are the weights penalizing control error and total thrust usage, respectively. The control wrench resulting from a given configuration is

$$\boldsymbol{u}_{\text{ctl}}(\boldsymbol{\theta}^*, \boldsymbol{f}^*) = [T(\boldsymbol{\theta}^*)]\boldsymbol{f}^* \tag{24}$$

where $[T(\boldsymbol{\theta}^*)] \in \mathbb{R}^{6\times N_T}$ is the joint configuration-dependent thruster mapping matrix

$$[T(\boldsymbol{\theta}^*)] = \begin{bmatrix} \hat{f}(\boldsymbol{\theta}^*)_1 \cdots \hat{f}(\boldsymbol{\theta}^*)_{N_T} \\ \boldsymbol{r}_{T_1/B}(\boldsymbol{\theta}^*) \times \hat{f}(\boldsymbol{\theta}^*)_1 \cdots \boldsymbol{r}_{T_{N_T}/B}(\boldsymbol{\theta}^*) \times \hat{f}(\boldsymbol{\theta}^*)_{N_T} \end{bmatrix} \tag{25}$$

where $\boldsymbol{r}_{T_1/B}(\boldsymbol{\theta}^*)$ is the position vector of the first thruster relative to point B for the desired configuration. The optimization problem is solved using the Sequential Least-Squares Programming (SLSQP) algorithm implemented in the *SciPy Python* package.

Under a zeroth-order hold assumption on the outer-loop command, each thruster's desired on-time is computed from the ratio of the desired force to its fixed output level, yielding

$$t_{i,\text{fire}} = \frac{f_i t_{\text{outer}}}{f_{i,\text{mag}}} \tag{26}$$

where f_i is the magnitude of the force for the ith thruster in vector $\boldsymbol{f}^*$, t_{outer} is the control period of the outer control loop, and $f_{i,\text{mag}}$ is the fixed thruster force for the ith thruster.

INNER CONTROL LOOP

While the outer control loop is responsible for ensuring the spacecraft achieves its mission-level objectives, the inner control loop governs the actuation of the arms and thrusters required to realize the outer-loop commands. This inner control loop is divided into two distinct phases: the first phase performs joint actuation, in which the arms are driven toward the desired joint angles determined by the optimization problem in the prior section. The second phase executes thruster firings for the commanded durations to produce the desired control wrench on the spacecraft.

The primary contribution of this work is the incorporation of a prescribed hub-torque term into the joint-actuation phase of the inner control loop in a 6-DOF spacecraft control architecture using of arm-mounted thrusters. This torque is computed in real time to counteract the reaction torques generated by joint motion. This enforces zero angular acceleration of the spacecraft hub during arm articulation, thereby maintaining sensor LOS. Prior proximity-operations control architectures that utilize arm mounted thrusters have either permitted hub attitude deviations during arm motion[20] or regulated the spacecraft attitude without formulating the reconfiguration phase as an explicit hub inverse-dynamics problem to enforce zero hub angular acceleration.[21]

Joint Actuation

The joint actuation phase of the inner-loop control is responsible for driving the joints to their desired angles and bringing them to rest at that commanded configuration, such that

$$\delta\boldsymbol{\theta} = \boldsymbol{\theta} - \boldsymbol{\theta}^* \to 0,\ \dot{\boldsymbol{\theta}} \to 0 \tag{27}$$

During the joint actuation phase, the thrusters are inactive, resulting in all thruster associated wrenches being zero. Additionally, a prescribed hub-torque $\boldsymbol{\tau}_{\text{pre}}$ is applied such that the hub angular acceleration satisfies $\dot{\boldsymbol{\omega}}_{B/N} = 0$. Unlike prior approaches that neglect sensor LOS requirements during reconfiguration, this formulation explicitly enforces zero hub angular acceleration. By enforcing this condition, the first and third equations in Eq. (1) is simplified to

$$M_{TT}\ddot{\boldsymbol{r}}_{B/N} + M_{T\theta}\ddot{\boldsymbol{\theta}} = -\boldsymbol{C}_T \tag{28a}$$
$$M_{T\theta}^T\ddot{\boldsymbol{r}}_{B/N} + M_{\theta\theta}\ddot{\boldsymbol{\theta}} = \boldsymbol{u}_J - \boldsymbol{C}_\theta \tag{28b}$$

Solving the Eq. (28a) for $\ddot{\boldsymbol{r}}_{B/N}$ yields

$$\ddot{\boldsymbol{r}}_{B/N} = -M_{TT}^{-1}(M_{T\theta}\ddot{\boldsymbol{\theta}} + \boldsymbol{C}_T) \tag{29}$$

Substituting this result into Eq. (28b) leads to

$$[\overline{M}]\ddot{\boldsymbol{\theta}} = \boldsymbol{u}_J - \overline{\boldsymbol{C}} \tag{30}$$

where

$$[\overline{M}] = M_{\theta\theta} - M_{T\theta}^T M_{TT}^{-1} M_{T\theta},\ \overline{\boldsymbol{C}} = \boldsymbol{C}_\theta - M_{T\theta}^T M_{TT}^{-1}\boldsymbol{C}_T \tag{31}$$

Because the system mass matrix $[M]$ is symmetric positive-definite (SPD), every principal submatrix of $[M]$ including those appearing in Eq. (28) is also SPD.[42] Consequently, the Schur complement $[\overline{M}]$ is SPD.[43]

Selecting the Lyapunov function

$$V(\delta\boldsymbol{\theta}, \dot{\boldsymbol{\theta}}) = \frac{1}{2}\dot{\boldsymbol{\theta}}^T\dot{\boldsymbol{\theta}} + \frac{1}{2}\delta\boldsymbol{\theta}^T[K_\theta]\delta\boldsymbol{\theta} \tag{32}$$

where $[K_\theta] \in \mathbb{R}^{N_J \times N_J}$ is a positive-definite gain matrix. Taking the derivative yields

$$\dot{V}(\delta\boldsymbol{\theta}, \dot{\boldsymbol{\theta}}) = \dot{\boldsymbol{\theta}}^T\left(\ddot{\boldsymbol{\theta}} + [K_\theta]\delta\boldsymbol{\theta}\right) \tag{33}$$

Forcing $\dot{V}$ to be negative-semidefinite by setting it equal to $\dot{V}(\delta\boldsymbol{\theta}, \dot{\boldsymbol{\theta}}) = -\dot{\boldsymbol{\theta}}^T [P_\theta]\dot{\boldsymbol{\theta}}$ where $[P_\theta] \in \mathbb{R}^{(N_J \times N_J)}$ is also a positive-definite gain matrix and substituting in $\ddot{\boldsymbol{\theta}}$ from Eq. (30) leads to

$$\dot{\boldsymbol{\theta}}^T \left[[\overline{M}]^{-1}(\boldsymbol{u}_J - \overline{\boldsymbol{C}}) + [P_\theta]\dot{\boldsymbol{\theta}} + [K_\theta]\delta\boldsymbol{\theta} \right] = 0 \tag{34}$$

Solving for the control by setting the term inside the brackets to zero yields the control

$$\boldsymbol{u}_J = [\overline{M}](-[K_\theta]\delta\boldsymbol{\theta} - [P_\theta]\dot{\boldsymbol{\theta}}) + \overline{\boldsymbol{C}} \tag{35}$$

This control law guarantees global stability since V is positive-definite and radially unbounded, and $\dot{V}$ is negative semi-definite. To prove asymptotic stability the methodology presented by Mukherjee and Chen[44] is employed. On the invariant set $\Omega = \{(\delta\boldsymbol{\theta}, \dot{\boldsymbol{\theta}}) : \dot{\boldsymbol{\theta}} = 0\}$, $\dot{V} = 0$. The second derivative of V is

$$\ddot{V} = -2\dot{\boldsymbol{\theta}}^T [P_\theta]\ddot{\boldsymbol{\theta}} \tag{36}$$

Since $\ddot{\boldsymbol{\theta}}$ is bounded under the globally stable control law, $\ddot{V} = 0$ on Ω. Taking the third derivative of V on Ω yields

$$\dddot{V} = -2 \left[(\boldsymbol{u}_J - \overline{\boldsymbol{C}})^T [\overline{M}]^{-1} [P_\theta][\overline{M}]^{-1}(\boldsymbol{u}_J - \overline{\boldsymbol{C}}) \right] \tag{37}$$

Substituting the value of the control derived in Eq. (35) and taking advantage of the SPD nature of $[\overline{M}]$ reduces the third derivative to

$$\dddot{V} = -2 \left[\delta\boldsymbol{\theta}^T [K_\theta]^T [P_\theta][K_\theta]\delta\boldsymbol{\theta} \right] \tag{38}$$

Because both $[K_\theta]$ and $[P_\theta]$ are positive-definite, $[K_\theta]^T [P]_\theta [K_\theta]$ is also positive definite resulting in $\dddot{V}$ being negative-definite in $\delta\boldsymbol{\theta}$. Therefore, the control $\boldsymbol{u}_J$ is globally asymptotically stabilizing.

With the joint control law established, the remaining task is to compute the prescribed hub torque $\boldsymbol{\tau}_{\text{pre}}$ that enforces the zero-angular-acceleration condition assumed throughout the joint actuation phase. Substituting the values of $\boldsymbol{u}_J$ into Eq. (30) produces the joint accelerations $\ddot{\boldsymbol{\theta}}$. These values can then be used in Eq. (29) to produce the hub translational acceleration. The corresponding instantaneous hub torque required to satisfy the rotational dynamics under the ideal control input assumption introduced in the *Control Architecture* section follows from Eq. (1) as

$$\boldsymbol{\tau}_{\text{pre}} = M_{TR}^T \ddot{\boldsymbol{r}}_{B/N} + M_{R\theta}\ddot{\boldsymbol{\theta}} + \boldsymbol{C}_R \tag{39}$$

Thruster Actuation

During the thruster firing phase of the inner control loop, the thrusters are commanded to generate the desired control wrench specified by the outer-loop controller. The prescribed hub torque is set to zero in this phase to allow the thrusters to generate the complete commanded control wrench. The joint motors, in turn, provide the necessary counteracting torques to offset the moments induced on the joints by the thruster firings, thereby maintaining $\ddot{\boldsymbol{\theta}} = 0$. Together with the zero joint velocities achieved during the preceding joint actuation phase, this condition ensures that the rigid-body assumptions underlying the outer-loop control remain valid during thruster execution.

Using Eq. (1) with $\boldsymbol{\tau}_{\text{pre}} = 0$ and $\ddot{\boldsymbol{\theta}} = 0$ produces

$$\begin{bmatrix} M_{TT} & M_{TR} \\ M_{TR}^T & M_{RR} \end{bmatrix} \begin{bmatrix} \ddot{\boldsymbol{r}}_{B/N} \\ \dot{\boldsymbol{\omega}}_{B/N} \end{bmatrix} + \begin{bmatrix} \boldsymbol{C}_T \\ \boldsymbol{C}_R \end{bmatrix} = \begin{bmatrix} \boldsymbol{F}_{\text{thr}} \\ \boldsymbol{L}_{\text{thr}} \end{bmatrix} \tag{40a}$$

$$M_{T\theta}^T \ddot{\boldsymbol{r}}_{B/N} + M_{R\theta}^T \dot{\boldsymbol{\omega}}_{B/N} + \boldsymbol{C}_\theta - \boldsymbol{\tau}_{\text{thr}} = \boldsymbol{u}_J \tag{40b}$$

Solving Eq. (40a) for $\ddot{\boldsymbol{r}}_{B/N}$ and $\dot{\boldsymbol{\omega}}_{B/N}$ and substituting the results into Eq. (40b) provides the joint torques required to nullify joint accelerations. The thruster-induced joint torques are defined as

$$\boldsymbol{\tau}_{\text{thr}} = [J]^T \boldsymbol{F} \tag{41}$$

where $[J] \in \mathbb{R}^{3N_T \times N_J}$ is the Jacobian mapping the forces generated by the thrusters, $\boldsymbol{F} \in \mathbb{R}^{3N_T}$, to the torques experienced at the joints.

SIMULATION AND RESULTS

Simulation Setup and Scenario Definition

In this section, the cascaded control outlined in the *Control Architecture* section and developed in the preceding sections is implemented in numerical simulation. To evaluate the proposed architecture in a representative proximity operations scenario that requires simultaneous translational tracking and precise LOS-constrained pointing, the relative motion inspection task shown in Fig. 6 is utilized. The simulated spacecraft consists of a 980 kg rectangular hub with dimensions $0.79 \times 0.69 \times 0.52$ m. The spacecraft has two identical arms mounted at centers of the $\pm\hat{b}_1$ face of the hub. Each arm is comprised of two segments: 1) joints 1 and 2 with the first boom, and 2) joints 3 and 4 with the second boom and the thruster. The properties of the arms are detailed in Table 1. The local spin axes of each joint are detailed in Table 2, the joints on each arm share identical spin axes. Each joint motor is capable of producing up to 2.5 Nm of torque. Each arm has a single thruster mounted at the end which produces a fixed 0.25 N of thrust and exerts the force along the local $[-1, 0, 0]^T$ direction. The control gains for the simulation are listed in Table 3.

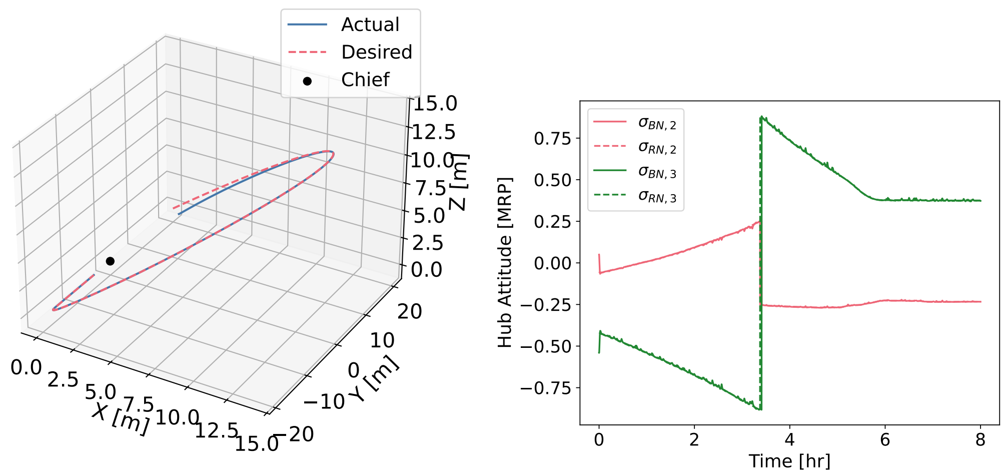

(a) Translational tracking performance

(b) Attitude tracking performance

Figure 6: Control tracking performance over 8 hr duration

Table 1: Arm parameters

Segment	Length	Mass	Inertia
1	1 m	8 kg	$\begin{bmatrix} 0.04 & 0 & 0 \\ 0 & 0.687 & 0 \\ 0 & 0 & 0.687 \end{bmatrix}$ kg·m^2
2	0.1 m	2 kg	$\begin{bmatrix} 0.0025 & 0 & 0 \\ 0 & 0.021 & 0 \\ 0 & 0 & 0.021 \end{bmatrix}$ kg·m^2

The multi-body spacecraft dynamics are simulated using the astrodynamics simulation framework Basilisk's implementation of MuJoCo*. An example implementation of a related regulation scenario using the Basilisk framework is available in the online documentation†. To isolate controller performance, the simulation is set

*`https://avslab.github.io/basilisk/Learn/makingModules/advancedTopics/mujocoDynObject.html`
†`https://avslab.github.io/basilisk/examples/mujoco/scenarioThrArmControl.html`

Table 2: Local joint spin axes

Joint	**1**	**2**	**3**	**4**
Spin axis	$[1,0,0]^T$	$[0,1,0]^T$	$[0,0,1]^T$	$[0,1,0]^T$

Table 3: Control gains

Gain	**Value**	**Gain**	**Value**
$[K_T]$ [N/m]	$0.02 \times [I_{3\times3}]$	$[P_T]$ [N·s/m]	$50 \times [I_{3\times3}]$
K_R [N·m]	1.75	$[P_R]$ [N·m·s]	$15.0 \times [I_{3\times3}]$
$[K_\theta]$ [N·m/rad]	$22 \times [I_{8\times8}]$	$[P_\theta]$ [N·m·s/rad]	$14 \times [I_{8\times8}]$

up in a gravity-free environment with no other external forces or torques. The outer control loop operates at 0.1 Hz, while the dynamics and inner control loop operate at 100 Hz. The joint angles are constrained to $(-\pi, \pi]$, and the maximum thrust is limited to $\boldsymbol{f}_{\text{max}} = 0.25$ N when using SLSQP to solve the joint and thruster allocation optimization problem. The weighting for the control errors and thruster forces during the optimization are 1.0 and 10^{-4} respectively. A simple rounding based firing algorithm[45] is used to turn thruster force request into on-times considering minimum thruster on-times and pulse resolution.

The spacecraft's initial conditions are $\boldsymbol{r}_{C/N}(t = 0) = [0.5, 19.65, -0.25]^T$ m, $\dot{\boldsymbol{r}}_{C/N}(t = 0) = [2.5 \times 10^{-3}, -4 \times 10^{-4}, 1.75 \times 10^{-3}]^T$ m/s, $\boldsymbol{\sigma}_{B/N}(t = 0) = [0.16, 0.05, -0.54]^T$, and $\boldsymbol{\omega}_{B/N}(t = 0) = [1.0 \times 10^{-3}, -2.5 \times 10^{-4}, -9.5 \times 10^{-4}]^T$ rad/s. All joint angles and velocities are initialized to zero. The goal of the simulation is for the spacecraft to fly the trajectory shown in Fig. 6a over an 8 hr time span while pointing its first body frame axis, $\hat{b}_1$, at the chief throughout the simulation*. It is important to note that Fig. 6b only displays the tracking about the second and third body axes because rotation about $\hat{b}_1$ does not contribute to pointing error. This first set of simulation results does not set limits on the deputy's prescribed hub torque generation.

Control Performance with Unconstrained Prescribed Hub Torque Authority

The performance of the proposed control architecture with no limits on prescribed hub torques is first evaluated. Figure 7 shows that the deputy's translational errors converge to zero within the first 3 hours of the simulation. After convergence, the position and velocity errors reach steady-state values of approximately 8 mm and 7 μm/s, respectively. Similarly, Fig. 8 shows the attitude errors converging to zero within the first 5 min of the simulation. After this point the controller is able to maintain an average pointing error of 0.57 deg and angular velocity error of 0.01 deg/s. Figure 8 shows some larger variation in both attitude and angular velocity errors; however, this is primarily due to the numerical differentiation used to generate the reference angular velocity. Unlike the attitude error the angular velocity error about $\hat{b}_1$ is included as the system is desired to be non-rotating about that axis.

Figure 9 illustrates the time required for arms to reach their desired configuration, defined as a max joint angle error of less than 1×10^{-3} rad and max joint velocity of less than 1×10^{-3} rad/s. As can be clearly seen, the majority of outer loop control periods settle in between 3s and 7s. Approximately 5% of cases do not settle within the 10 s outer control loop period, resulting in no thruster firing during that cycle. Almost 90% of the cases that do not settle correspond with more than half of the joints being required to reorient in excess of 100 deg. Despite this, approximately 65% of these non-settling cases are still able to fire the thrusters in the next control period. As shown by Figs. 7 and 8 these missed firing times do not result in meaningful tracking errors. When comparing these settling times with the thruster on-time requests in Fig. 10 it is clear that the thrusters are able to complete their requested firing times the vast majority of the time.

*`https://avslab.github.io/basilisk/Documentation/fswAlgorithms/attGuidance/locationPointing/locationPointing.html`

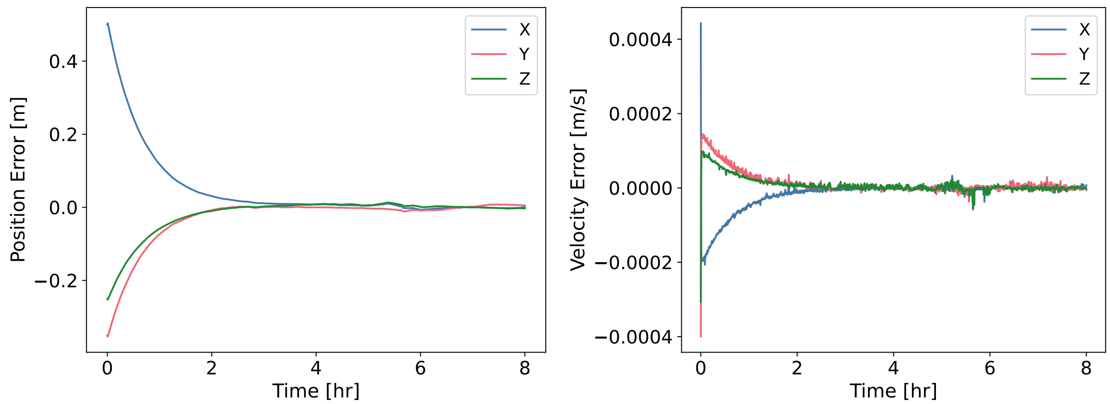

(a) Position error

(b) Velocity error

Figure 7: Translational error for the system CoM

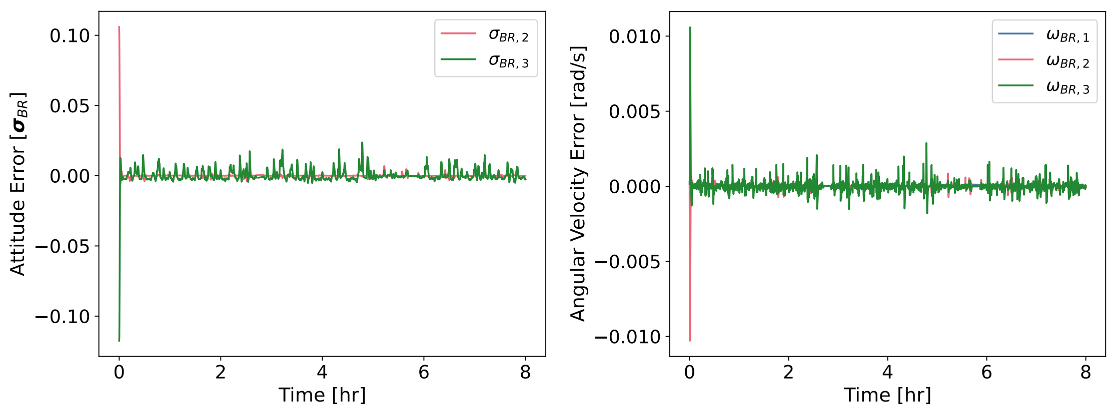

(a) Attitude error $\boldsymbol{\sigma}_{B/R}$

(b) Angular velocity error $\boldsymbol{\omega}_{B/R}$

Figure 8: Rotational error for the spacecraft hub

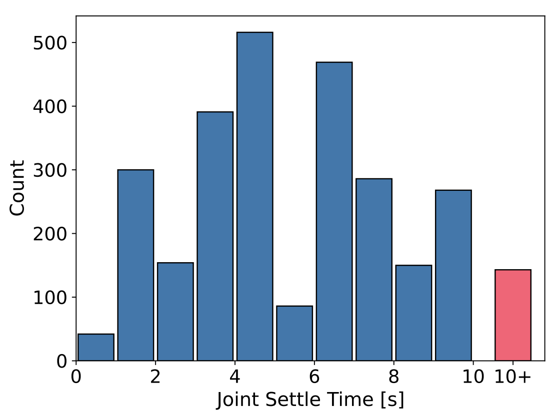

Figure 9: Time taken for joints to settle at desired values

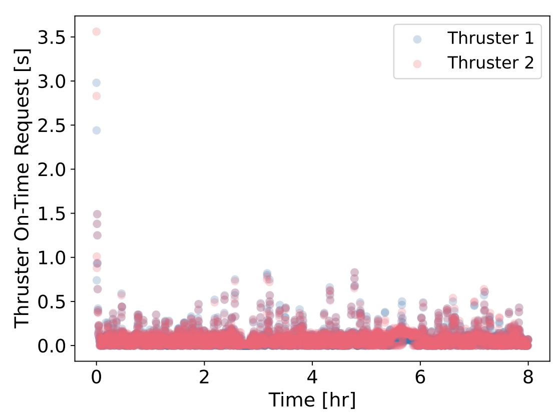

Figure 10: Requested thruster firing time

The prescribed hub torques required to prevent hub acceleration during arm articulation are shown in Fig. 11. The required hub torques exhibit large transient peaks, particularly about $\hat{b}_2$ and $\hat{b}_3$, demonstrating that rapid arm articulation induces significant instantaneous reaction torques on the hub. These results highlight the need for a subsystem capable of counteracting the reaction torques; without compensation, the hub would experience large angular accelerations that degrade the performance of the relative motion sensors mounted to the spacecraft hub. However, these peaks are short-lived, often decaying to just 10-20$\%$ of their maximum value in fractions of a second, as shown by Fig. 11b. This behavior suggests that saturation of the prescribed hub torques may provide a practical implementation strategy, enabling reduced actuator requirements while maintaining acceptable pointing performance.

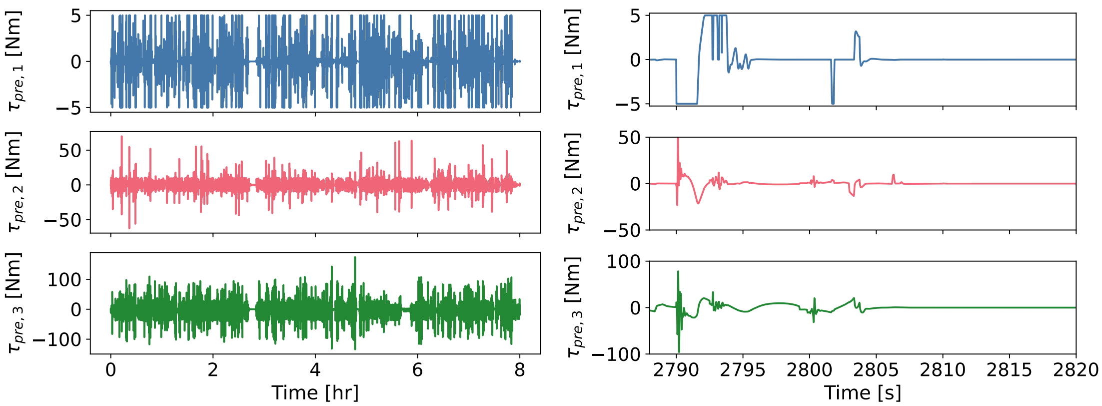

(a) Prescribed torque over full simulation time

(b) Prescribed torque between $t = 2788$ s and $t = 2820$ s

Figure 11: Prescribed hub torques required to offset arm motion

Control Performance with Limited Prescribed Hub Torque Authority

Due to the short-lived but extreme prescribed hub torque demands observed in the previous results, the feasibility of the control architecture under limited hub torque authority is investigated next. To accomplish this, the prescribed torque along each body axis is limited to 20 Nm. This value represents the torque that could reasonably be produced by a multi-CMG cluster of commercially available products*. All other parameters are kept identical to the prior simulation. For this work, a camera half angle of 20 deg is chosen as the conservative metric for maintaining LOS based on prior wide FOV relative motion cameras.[46]

As expected, the limitations on prescribed hub torque show a minimal impact on the translational portion of the controller as demonstrated by Fig. 12 marginally reducing steady state errors. Figure 13a demonstrates the hub is able to track the pointing orientation throughout the simulation despite the limit of the prescribed hub torque. The attitude controller experiences more chatter than the case with no limits in Fig. 6b, as is to be expected due to the lack of ideal reaction torque cancellation. Figure 13b shows the amount of time spent at a given pointing error throughout the simulation. When subjected to the torque limits the average pointing error grows to 3.52 deg and average angular velocity error is 0.1 deg/s, much higher than in the uncapped case, however, over 70$\%$ of the simulation duration is spent at below 5 deg of pointing error. After the initial pointing error is eliminated, more than 99.9$\%$ of the remaining nearly 8 hr of the simulation is spent with a pointing error below the 20 deg camera half-angle. Thus, although a single brief LOS violation occurs, LOS-constrained pointing is effectively maintained for the vast majority of the simulation despite the limitations placed on the prescribed hub torque. Therefore, despite the saturation of the prescribed hub torque, the controller maintains LOS-constrained pointing, demonstrating the robustness of the control architecture to actuator limitations.

*https://www.bluecanyontech.com/components/control-moment-gyroscopes/

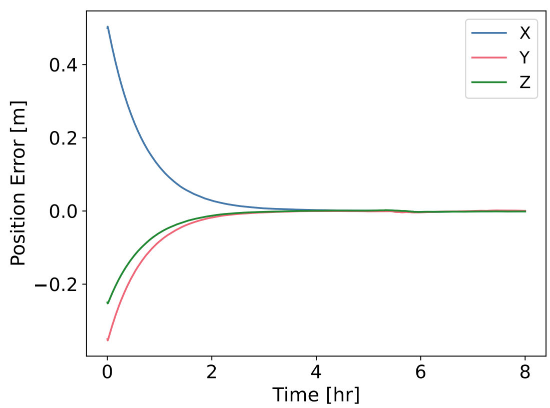

(a) Position error

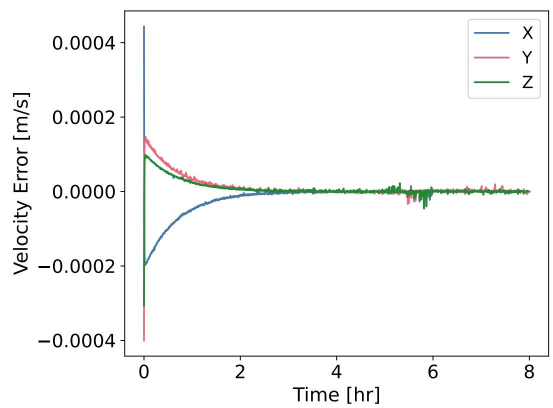

(b) Velocity error

Figure 12: Translational error for the system CoM with hub torque limits

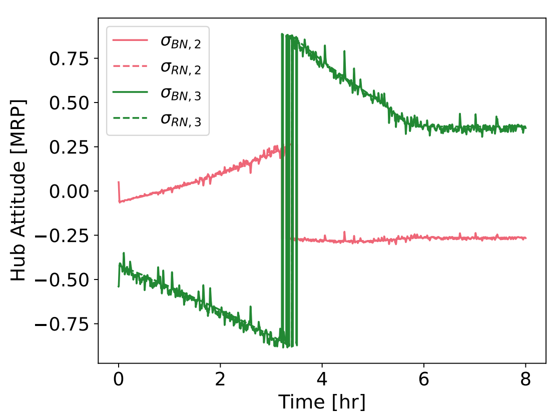

(a) Attitude tracking performance

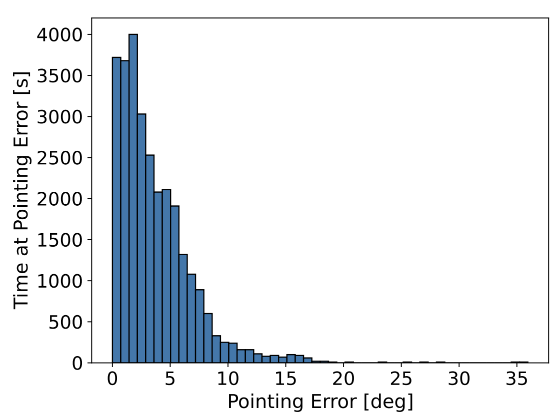

(b) Time at a given pointing error

Figure 13: Rotational tracking performance with hub torque limits

Control Performance Under Hub-Inertia-Dominant Modeling Assumption

As discussed in the *Rotational Control* section, the outer-loop rotational control law makes the simplifying assumption that the total spacecraft inertia is dominated by the static rigid hub inertia. This section aims to investigate this assumption by evaluating the control performance for different arm-to-hub mass ratios. To evaluate this, control performance for arm-to-hub mass ratios of Case 1 (0.1) and Case 2 (0.2) is compared to the base case (~ 0.0204) discussed in the unconstrained results section. For each simulation the hub mass and inertia are kept identical to the base case as are the arm dimensions. The mass of each arm segment is then scaled according to the specified arm-to-hub mass ratio. The parameters in Table 4 are varied to keep the translational performance as close to the base case as possible as well as force the joint settling behavior to be close to the base case. This resulted in the steady state position error decreasing by 4-6 mm and velocity errors decreasing by 2-3 μm/s. Similarly, the percent of episodes where the joints do not settle varied by less than 0.2% in both cases and the median settling time improved by 0.3-0.5 s.

Table 4: Parameters for varied arm-to-hub mass ratio trials

Parameter	Case 1	Case 2
Total Mass [kg]	1078	1176
Thruster force [N]	0.2695	0.294
$[K_T]$ [N/m]	$0.02156 \times [I_{3\times3}]$	$0.022352 \times [I_{3\times3}]$
$[P_T]$ [N·s/m]	$53.9 \times [I_{3\times3}]$	$58.8 \times [I_{3\times3}]$
Max Motor Torque [N·m]	11.75	23.5
$[K_\theta]$ [N·m/rad]	$22.5 \times [I_{8\times8}]$	$21 \times [I_{8\times8}]$
$[P_\theta]$ [N·m·s/rad]	$14.25 \times [I_{8\times8}]$	$13.5 \times [I_{8\times8}]$

While the translational and joint performance are tuned to maintain comparable performance across trials, the attitude-pointing response varies significantly with arm-to-hub mass ratio. As shown in Fig. 14 Case 1 exhibits slightly larger transients than the base case but converges on a similar timescale. In contrast, Case 2 shows substantially larger transients and a longer convergence time. All three cases also exhibit an error-growth region around $t \approx 8 - 12$ min. The amplitude and duration of this secondary response increase with mass ratio, with Case 2 showing the largest and most persistent deviations.

To quantify these time-history trends, Fig. 15 summarizes the pointing- and rate-error distributions after the initial errors have been resolved (final 90% of simulation duration). Both Case 1 and 2 degrade relative to the base case in both pointing- and rate-error, with Case 2 showing substantial degradation: even its lower quartile exceeds most of the non-outlier data from the base case. In addition, Case 2 contains post-transient outliers that begin to violate the previously established LoS constraint. These results indicate that the hub-inertia-dominant assumption in the *Rotational Control* section remains effective over a nontrivial range of arm-to-hub mass ratios, but its robustness degrades as the ratio increases.

CONCLUSIONS

This paper develops a cascaded control architecture that incorporates a prescribed hub-torque term computed in real time to counteract reaction torques generated during arm motion, enabling 6-DOF spacecraft control using thrusters mounted on robotic arms while reducing the number of required thrusters and leveraging existing manipulator systems. This formulation prevents loss of pointing LOS during arm reconfiguration, ensuring that the chief spacecraft remains within the deputy's FOV despite rapid joint motion.

Simulation results of a relative motion inspection scenario demonstrate that the proposed control architecture can achieve simultaneous translational tracking and attitude pointing throughout the maneuver using only two arm-mounted thrusters. While the unconstrained prescribed hub-torque demands are shown to be large, additional simulations demonstrate that the proposed controller remains effective when torque authority is limited to levels achievable by commercially available multi-CMG clusters. Finally, the controller is shown to remain viable under a hub-inertia dominant modeling assumption and to retain acceptable performance

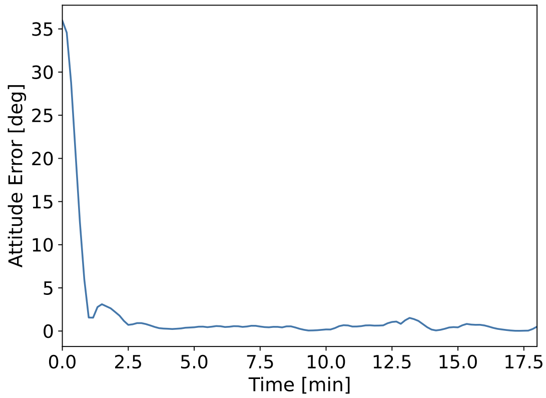

(a) Base case

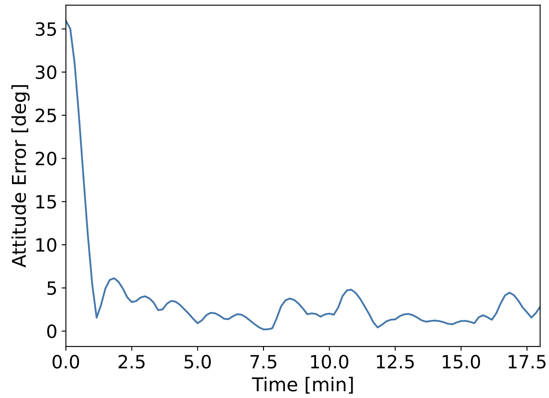

(b) Case 1: arm-to-hub mass ratio = 0.1

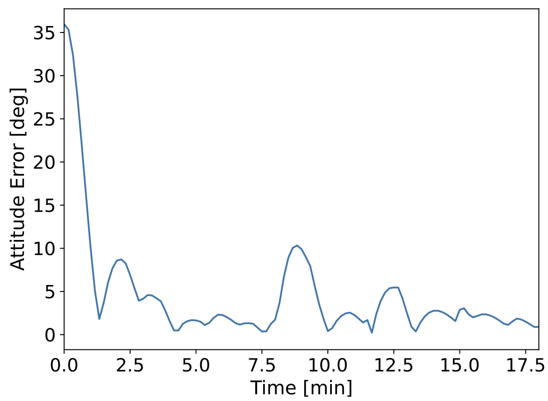

(c) Case 2: arm-to-hub mass ratio = 0.2

Figure 14: Spacecraft hub pointing error for first 18 min of simulation

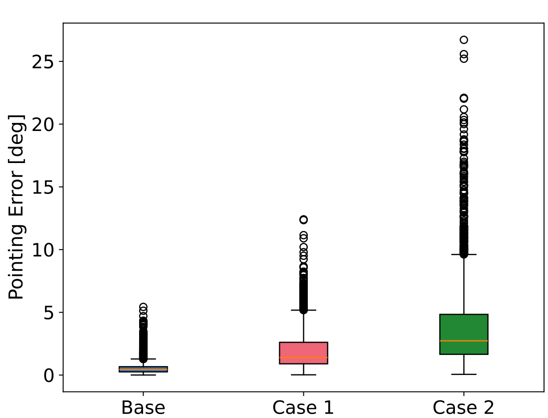

(a) Pointing error

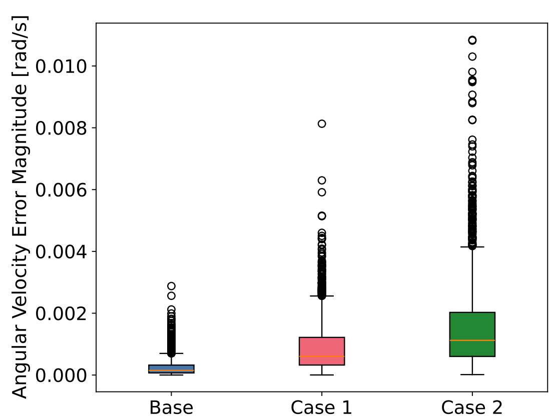

(b) Angular velocity error

Figure 15: Attitude tracking performance throughout final 90% of simulation

over a nontrivial range of arm-to-hub mass ratios. These results demonstrate that arm-mounted thrusters, when paired with real-time reaction torque compensation, offer a viable path toward reduced-actuator 6-DOF control architectures for future proximity operations and ISAM missions.

Disclaimer

The views expressed in this article are those of the author and do not reflect the official policy or position of the United States Space Force, Department of Defense, or the U.S. Government.

REFERENCES

[1] R. Mukherjee, "Survey Of Select Recent In-Space Servicing Assembly and Manufacturing Related Robotics Projects at The Jet Propulsion Laboratory," *ASCEND 2023*, Las Vegas, Nevada, American Institute of Aeronautics and Astronautics, Oct. 2023, 10.2514/6.2023-4700.

[2] D. D. Arney, J. Mulvaney, C. Williams, W. Ruperto-Hernández, J. Friz, C. Stockdale, J. Nelson, and R. Rivera-Vargas, "In-Space Servicing, Assembly, and Manufacturing (ISAM) State of Play," 2024.

[3] J. Lawless, S. Patane, R. Rollins, M. Ledbetter, and R. Cook, "Future ISAM Architectures for National Security Space," *ASCEND 2022*, Las Vegas, Nevada & Online, American Institute of Aeronautics and Astronautics, Oct. 2022, 10.2514/6.2022-4299.

[4] J. N. Opiela, "Orbital Debris Charts, April 2024," Apr. 2024.

[5] J. Rudico, J. T. Nichols, and G. Rogers, "Potential United States Space Force Mission Life Extension Applications," *AIAA SCITECH 2024 Forum*, Orlando, FL, American Institute of Aeronautics and Astronautics, Jan. 2024, 10.2514/6.2024-1067.

[6] J. L. Goodman, "History of Space Shuttle Rendezvous and Proximity Operations," *Journal of Spacecraft and Rockets*, Vol. 43, Sept. 2006, pp. 944–959, 10.2514/1.19653.

[7] M. Pasand, A. Hassani, and M. Ghorbani, "A Study of Spacecraft Reaction Thruster Configurations for Attitude Control System," *IEEE Aerospace and Electronic Systems Magazine*, Vol. 32, July 2017, pp. 22–39, 10.1109/MAES.2017.160104.

[8] J. H. Meub, "Continuous Low Thrust for Small Spacecraft Proximity Operations," Master's thesis, Missouri University of Science and Technology, 2011.

[9] P. Z. Schulte and D. A. Spencer, "Development of an Integrated Spacecraft Guidance, Navigation, & Control Subsystem for Automated Proximity Operations," *Acta Astronautica*, Vol. 118, Jan. 2016, pp. 168–186, 10.1016/j.actaastro.2015.10.010.

[10] F. Curti, M. Romano, and R. Bevilacqua, "Lyapunov-Based Thrusters' Selection for Spacecraft Control: Analysis and Experimentation," *Journal of Guidance, Control, and Dynamics*, Vol. 33, July 2010, pp. 1143–1160, 10.2514/1.47296.

[11] M. Wang and Y. Xie, "Design of the Optimal Thruster Combinations Table for the Real Time Control Allocation of Spacecraft Thrusters," *Proceedings of the 48h IEEE Conference on Decision and Control (CDC) Held Jointly with 2009 28th Chinese Control Conference*, Dec. 2009, pp. 5063–5068, 10.1109/CDC.2009.5400664.

[12] F. Schmucker, "Development and Validation of an Efficient Thruster-Based Control Strategy for Orbital Robots," Master's thesis, Technical University of Munich, 2020.

[13] S.-z. Yang, L. Wang, and P. Sun, "Optimal Thrust Allocation Logic Design of Dynamic Positioning with Pseudo-Inverse Method," *Journal of Shanghai Jiaotong University (Science)*, Vol. 16, Feb. 2011, pp. 118–123, 10.1007/s12204-011-1104-9.

[14] M. Fauré, D. Henry, J. Cieslak, P. Lachevre, and F. Ankersen, "Optimization of Spacecraft Thrusters Configuration Under Fault Diagnosability and Recoverability Constraints," *IEEE Transactions on Aerospace and Electronic Systems*, Vol. 59, Oct. 2023, pp. 5275–5286, 10.1109/TAES.2023.3256976.

[15] D. Zlotnik, S. Di Cairano, and A. Weiss, "MPC for Coupled Station Keeping, Attitude Control, and Momentum Management of GEO Satellites Using on-off Electric Propulsion," *2017 IEEE Conference on Control Technology and Applications (CCTA)*, Aug. 2017, pp. 1835–1840, 10.1109/CCTA.2017.8062723.

[16] R. J. Caverly, S. Di Cairano, and A. Weiss, "Split-Horizon MPC for Coupled Station Keeping, Attitude Control, and Momentum Management of GEO Satellites Using Electric Propulsion," *2018 Annual American Control Conference (ACC)*, June 2018, pp. 652–657, 10.23919/ACC.2018.8431329.

[17] R. J. Caverly, S. Di Cairano, and A. Weiss, "On-Off Quantization of an MPC Policy for Coupled Station Keeping, Attitude Control, and Momentum Management of GEO Satellites," *2018 European Control Conference (ECC)*, June 2018, pp. 1–6, 10.23919/ECC.2018.8550336.

[18] R. Caverly, S. Di Cairano, and A. Weiss, “Control Allocation and Quantization of a GEO Satellite with 4DOF Gimbaled Thruster Booms,” *AIAA Scitech 2020 Forum*, Orlando, FL, American Institute of Aeronautics and Astronautics, Jan. 2020, 10.2514/6.2020-1687.

[19] Z. Wei, T. Long, R. Shi, and X. Song, “Electric Thruster Configuration Design Optimization for Geostationary Satellites with Robotic Manipulators,” *Advances in Space Research*, Vol. 69, May 2022, pp. 3798–3813, 10.1016/j.asr.2022.02.048.

[20] A. Prakash and D. K. Giri, “Design and Dynamical Analysis of a Novel 6-DOF Spacecraft Maneuvering System Using Robotic Manipulator-Based Thruster System,” *AIAA SCITECH 2025 Forum*, Orlando, FL, American Institute of Aeronautics and Astronautics, Jan. 2025, 10.2514/6.2025-0408.

[21] F. Sena, R. Vijayan, H. Mishra, and M. D. Stefano, “Center-of-Mass and Attitude Control of an Orbital Manipulator: A Novel Control Strategy,” *IEEE Robotics and Automation Letters*, Vol. 11, June 2026, pp. 6871–6878, 10.1109/LRA.2026.3682621.

[22] W. R. Schwend and H. Schaub, “Planar Spacecraft Control Through One Degree of Freedom Time-varying Thruster Configurations,” *AAS/AIAA Astrodynamics Specialist Conference*, Aug. 2025.

[23] P. Th. L. M. van Woerkom and A. K. Misra, “Robotic Manipulators in Space: A Dynamics and Control Perspective,” *Acta Astronautica*, Vol. 38, Feb. 1996, pp. 411–421, 10.1016/0094-5765(96)00018-5.

[24] S. A. A. Moosavian and E. Papadopoulos, “Free-Flying Robots in Space: An Overview of Dynamics Modeling, Planning and Control,” *Robotica*, Vol. 25, Sept. 2007, pp. 537–547, 10.1017/S0263574707003438.

[25] P. Efimova and D. Shymanchuk, “Dynamic Model of Space Robot Manipulator,” *Applied Mathematical Sciences*, Vol. 9, 2015, pp. 4653–4659, 10.12988/ams.2015.56429.

[26] M. Oda, “Coordinated Control of Spacecraft Attitude and Its Manipulator,” *Proceedings of IEEE International Conference on Robotics and Automation*, Vol. 1, Apr. 1996, pp. 732–738 vol.1, 10.1109/ROBOT.1996.503861.

[27] L. Shi, J. Katupitiya, and N. Kinkaid, “A Robust Attitude Controller for a Spacecraft Equipped with a Robotic Manipulator,” *2016 American Control Conference (ACC)*, July 2016, pp. 4966–4971, 10.1109/ACC.2016.7526140.

[28] I. M. Da Fonseca, L. C. S. Goes, N. Seito, M. K. da Silva Duarte, and É. J. de Oliveira, “Attitude Dynamics and Control of a Spacecraft like a Robotic Manipulator When Implementing On-Orbit Servicing,” *Acta Astronautica*, Vol. 137, Aug. 2017, pp. 490–497, 10.1016/j.actaastro.2016.12.020.

[29] A. Antonello, A. Valverde, and P. Tsiotras, “Dynamics and Control of Spacecraft Manipulators with Thrusters and Momentum Exchange Devices,” *Journal of Guidance, Control, and Dynamics*, Vol. 42, No. 1, 2019, pp. 15–29, 10.2514/1.G003601.

[30] L. Shi, H. Jayakody, J. Katupitiya, and X. Jin, “Coordinated Control of a Dual-Arm Space Robot: Novel Models and Simulations for Robotic Control Methods,” *IEEE Robotics & Automation Magazine*, Vol. 25, Dec. 2018, pp. 86–95, 10.1109/MRA.2018.2864717.

[31] F. Basana, Z. Pavanello, F. Branz, A. Francesconi, G. Borelli, D. Invernizzi, M. Massari, M. Lovera, A. Nocerino, R. Opromolla, I. Huertas Garcia, and P. Simplicio, “Satellite and Robotic Arm Combined Control for Spacecraft Close-Proximity Operations,” *CEAS Space Journal*, Vol. 17, Mar. 2025, pp. 309–335, 10.1007/s12567-024-00560-0.

[32] X.-F. Liu, H.-Q. Li, Y.-J. Chen, G.-P. Cai, and X. Wang, “Dynamics and Control of Capture of a Floating Rigid Body by a Spacecraft Robotic Arm,” *Multibody System Dynamics*, Vol. 33, Mar. 2015, pp. 315–332, 10.1007/s11044-014-9434-7.

[33] R. Featherstone, *Rigid Body Dynamics Algorithms*. Boston, MA: Springer, 2008, 10.1007/978-1-4899-7560-7.

[34] E. Todorov, T. Erez, and Y. Tassa, “MuJoCo: A Physics Engine for Model-Based Control,” *2012 IEEE/RSJ International Conference on Intelligent Robots and Systems*, Oct. 2012, pp. 5026–5033, 10.1109/IROS.2012.6386109.

[35] T. F. Wiener, *Theoretical Analysis of Gimballess Inertial Reference Equipment Using Delta-Modulated Instruments*. Ph.D. dissertation, Department of Aeronautics and Astronautics, Massachusetts Institute of Technology, Cambridge, MA, March 1962.

[36] S. R. Marandi and V. J. Modi, “A Preferred Coordinate System and the Associated Orientation Representation in Attitude Dynamics,” *Acta Astronautica*, Vol. 15, No. 11, 1987, pp. 833–843.

[37] M. D. Shuster, “A Survey of Attitude Representations,” *Journal of the Astronautical Sciences*, Vol. 41, No. 4, 1993, pp. 439–517.

[38] H. Schaub and J. L. Junkins, *Analytical Mechanics of Space Systems*. Reston, VA: AIAA Education Series, 4th ed., 2018, 10.2514/4.105210.

[39] T. Yamamoto, H. Okamoto, M. Tomitaka, R. Nakamura, and Y. Takeuchi, “Advancing Active Debris Removal: Achievements and Prospects in the Commercial Removal of Debris Demonstration Project,” *9th European Conference on Space Debris*, Bonn, Germany, 2025.

[40] A. Weiss, X. Yang, I. Kolmanovsky, and D. S. Bernstein, "Inertia-Free Spacecraft Attitude Control Using Reaction Wheels," *AIAA Guidnace, Navigation, and Control Conference*, Toronto, Ontario, Canada, Aug. 2010, 10.2514/1.58363.

[41] H. Schaub, M. Akella, and J. L. Junkins, "Adaptive Control of Nonlinear Attitude Motions Realizing Linear Closed Loop Dynamics," *Journal of Guidance, Control and Dynamics*, Vol. 24, January–February 2001, pp. 95–100, 10.2514/2.4680.

[42] W. K. Nicholson, *Linear Algebra With Applications*. 2019.

[43] S. P. Boyd and L. Vandenberghe, *Convex Optimization*. Cambridge New York Melbourne New Delhi Singapore: Cambridge University Press, version 29 ed., 2023.

[44] R. Mukherjee and D. Chen, "Asymptotic Stability Theorem for Autonomous Systems," *Journal of Guidance, Control, and Dynamics*, Vol. 16, Sept. 1993, pp. 961–963, 10.2514/3.21108.

[45] J. Alcorn, H. Schaub, and S. Piggott, "Steady-State Attitude and Control Effort Sensitivity Analysis of Discretized Thruster Implementations," *Journal of Spacecraft and Rockets*, Vol. 54, Sept. 2017, pp. 1161–1169, 10.2514/1.A33709.

[46] J. Galante, J. Van Eepoel, M. Strube, N. Gill, M. Gonzalez, A. Hyslop, and B. Patrick, "Pose Measurement Performance of the Argon Relative Navigation Sensor Suite in Simulated-Flight Conditions," *AIAA Guidance, Navigation, and Control Conference*, Minneapolis, Minnesota, American Institute of Aeronautics and Astronautics, Aug. 2012, 10.2514/6.2012-4927.

APPENDIX: TRANSLATIONAL RELATIVE MOTION CONTROL STABILITY PROOF

The control law in Eq. (17) is globally asymptotically stabilizing, as shown below using the Lyapunov function defined in Eq. (15). Because the Lyapunov function is positive definite and radially unbounded while its derivative Eq. (16) is negative semi-definite, the control law is globally stabilizing.

To establish the asymptotically stability, we evaluate higher-order derivatives of V on the set where $\dot{V} = 0$, defined as

$$\Omega = \big\{ (\Delta \boldsymbol{r}, \Delta \dot{\boldsymbol{r}}) \,\big|\, \Delta \dot{\boldsymbol{r}} = \boldsymbol{0} \big\}. \tag{42}$$

Evaluating the second derivative of V on Ω results in $\ddot{V} = 0$, as the value of $\Delta \ddot{\boldsymbol{r}}$ is bounded due to the stabilizing nature of the control. The third derivative of V on Ω is found to be

$$\dddot{V} = -\frac{2}{m_d} \Delta \boldsymbol{r}^T [K_T]^T [P_T][K_T] \Delta \boldsymbol{r} \tag{43}$$

Because both $[K_T]$ and $[P_T]$ are positive definite, the matrix $[K_T]^T [P_T][K_T]$ is also positive definite, therefore $\dddot{V}$ on Ω is negative definite in $\Delta \boldsymbol{r}$. Since the first non-zero derivative is of an odd order and is negative definite in $\Delta \boldsymbol{r}$, the theorem by Mukherjee and Chen[44] establishes the control as globally asymptotically stabilizing.